# A Fast, Accurate, and Reactive Equivariant Foundation Potential

Tsz Wai Ko,\* Runze Liu, Adesh Rohan Mishra, Zihan Yu, Ji Qi, and Shyue Ping

Ong\*

Aiiso Yufeng Li Family Department of Chemical and Nano Engineering, University of California San Diego, 9500 Gilman Dr, Mail Code 0448, La Jolla, CA 92093-0448, United States

E-mail: t1ko@ucsd.edu; ongsp@ucsd.edu

#### Abstract

Electrostatics govern charge transfer and reactivity in materials. Yet, most foundation potentials (FPs) either do not explicitly model such interactions or pay a prohibitive scaling penalty to do so. Here, we introduce charge-equilibrated TensorNet (QET), an equivariant, charge-aware architecture that attains linear scaling with system size via an analytically solvable charge-equilibration scheme. We demonstrate that a trained QET FP matches state-of-the-art FPs on standard materials property benchmarks but delivers qualitatively different predictions in systems dominated by charge transfer. The QET FP reproduces the correct structure and density of the NaCl-CaCl<sub>2</sub> ionic liquid, which charge-agnostic FPs miss. We further show that a fine-tuned QET captures reactive processes at the  ${\rm Li/Li_6PS_5Cl}$  solid-electrolyte interface and supports simulations under applied electrochemical potentials. These results remove a fundamental constraint in the atomistic simulation of accurate electrostatics at scale and establish a general, data-driven framework for charge-aware FPs with transformative applications in energy storage, catalysis, and beyond.

## Introduction

Modeling electrostatics is essential to describe charge transfer, reactivity, and non-bonded interactions in molecules and materials. Although ab initio methods such as density functional theory (DFT) can accurately capture these interactions, their prohibitive computational cost and poor scaling (typically  $\geq \mathcal{O}(N_e^3)$ , where  $N_e$  is the number of electrons) render them impractical for large length and long time scale simulations.

Machine learning interatomic potentials (MLIPs)<sup>1</sup> represent a modern approach to overcome the accuracy-cost tradeoffs in traditional simulation approaches. MLIPs utilize an ML model to reproduce the potential energy surface (PES) from ab initio training data, providing accurate energy, force, and stress predictions at a fraction of the computational cost and linear scaling with respect to the number of atoms ( $\mathcal{O}(N_{atoms})$ ), where  $N_{atoms}$  is the number of atoms). A particularly exciting development in recent years is the concept of foundation potentials (FPs),<sup>2</sup> which are universal MLIPs that have comprehensive coverage of the periodic table. With rapid progress,<sup>3-6</sup> pre-trained FPs today can serve as surrogates for expensive DFT calculations in many applications, most notably in materials discovery where the ability to rapidly screen vast chemical spaces is a key requirement.

However, most MLIPs and FPs are limited in their ability to describe electrostatic interactions. Although graph-based MLIPs, such as the Materials 3-body Graph Network (M3GNet),<sup>2</sup> Message-passing Atomic Cluster Expansion (MACE),<sup>4</sup> and Graph Atomic Cluster Expansion (GRACE),<sup>6</sup> can in principle extend the range of interactions by increasing the number of message-passing steps, this approach is inefficient and leads to a computationally prohibitive increase in the number of model parameters. Furthermore, increasing the number of interaction blocks may degrade the accuracy of the model due to over-smoothing and over-squashing.<sup>7</sup> Despite its acronym, it should be noted that the Crystal Hamiltonian Graph Network (CHGNet)<sup>3</sup> architecture does not capture electrostatics but rather regularizes model training using magnetic moments as a proxy for the oxidation state.

A common approach to address this long-standing challenge is to incorporate the charge

equilibration (Qeq) scheme of Rappe and Goddard III<sup>8</sup> into MLIPs. <sup>9,10</sup> The general concept is to learn environment-dependent atomic electronegativities and hardnesses to distribute charges across the entire system so that the Qeq energy expression is minimized. These charges can then be used to calculate electrostatic interactions using Coulomb's law. Over the past few years, Qeq-based MLIPs, such as the fourth-generation high-dimensional neural network potential (4G-HDNNP), <sup>11,12</sup> atoms-in-molecules neural network with neural spin equilibration (AIMNet-NSE), <sup>13</sup> and others, <sup>14–17</sup> have been developed to describe non-local charge transfer and multiple charge states for applications such as protonation/deprotonation of molecules and electrocatalysis. Some alternative approaches, such as global attention, <sup>18</sup> maximally localized Wannier function centers (MLWCs), <sup>19</sup> latent Ewald summation-based methods <sup>20</sup> and latent message passing, <sup>21</sup> can also accurately describe electrostatic interactions without explicit charge training.

Despite these promising advances, developing an FP for materials that can accurately capture non-local charge transfer across the periodic table remains an open challenge. This is primarily due to the lack of large-scale reference datasets with reliable partial charges and higher-order multipoles. Modern PES-quality datasets, such as the Materials Potential Energy Surface (MatPES)<sup>22</sup> and OMat24<sup>23</sup> datasets, currently do not provide this information. Additionally, most Qeq implementations rely on solving systems of linear equations to capture global charge distributions, which leads to a cubic, or at best quadratic, scaling with respect to the number of atoms due to the nested computation loops during elimination or factorization.

In this work, we introduce a fast, accurate, and reactive equivariant FP based on a charge-equilibrated TensorNet<sup>24</sup> (QET, pronounced as "ket") architecture. QET attains linear scaling with system size by replacing conventional electrostatic solvers with an analytically solvable charge-equilibration scheme, while maintaining high accuracy in the PES and predicted atomic charges. We demonstrate that QET captures charge transfer and multiple charge states across diverse model systems. To train QET, we constructed MatQ, a

large charge-informed dataset comprising configurations sampled from structural deformations and high-temperature ab initio molecular dynamics (AIMD), spanning 86 elements of the periodic table. We show that the QET FP compares favorably with the state-of-the-art FPs<sup>6,25</sup> in near-equilibrium property benchmarks. Finally, we show that QET can be efficiently fine-tuned for complex reactive environments, such as the electrode/solid-electrolyte interface in next-generation all-solid-state lithium-ion batteries.

## Results

### **QET** architecture

The QET architecture is based on TensorNet,  $^{24}$  which has been shown to achieve significantly improved parameter and computational efficiency compared to other equivariant graph deep learning architectures by using Cartesian rank-2 tensor atomic embeddings. The Qeq scheme has been extensively detailed in previous work,  $^{8,11,13,14}$  and an overview is provided in the Supplementary Information. Solving the Qeq system of linear equations using naive methods such as QR or LU decomposition results in  $\mathcal{O}(N_{atoms}^3)$  scaling. Additionally, for periodic systems, setting up these equations involves computing the electrostatic energy via an Ewald summation, which scales from  $\mathcal{O}(N_{atoms}^{1.5})$  in the best case, to  $\mathcal{O}(N_{atoms}^2)$  in the worst case, depending on the choice of splitting parameters. Despite advances in optimization techniques,  $^{26}$  it remains prohibitively expensive to train a Qeq FP using large datasets or to perform large-scale simulations.

The schematic of the QET architecture is shown in Fig. 1. To develop a linear-scaling charge equilibration (LQeq) scheme, we take inspiration from traditional mean-field approaches such as the Hartree-Fock method, but modernized to exploit machine learning approaches to mapping non-linear relationships. We introduce an effective electronegativity

 $\chi_i^{\prime}$ , 15,27 defined as follows:

$$\chi_i' = \chi_i + \frac{q_i}{2\sigma_i \sqrt{\pi}} + \sum_{i>j}^{N_{\text{atoms}}} \frac{\operatorname{erf}\left(\frac{R_{ij}}{\sqrt{2(\sigma_i^2 + \sigma_j^2)}}\right)}{R_{ij}} q_j, \tag{1}$$

Here,  $\chi_i$  is the electronegativity in the standard Qeq scheme,  $\sigma_i$  and  $\sigma_j$  denote the width of the Gaussian-distributed charges,  $q_i$  represents the partial charge of atom i, and  $R_{ij}$  is the distance between atoms i and j.

The partial charges  $q_i$  are then given by an elegant analytic solution in terms of the effective electronegativities  $\chi'_i$  and hardnesses  $\eta_i$ , as follows:

$$q_{i} = -\eta_{i}^{-1} \left[ \chi_{i}' - \frac{Q_{\text{tot}} + \sum_{i=1} \chi_{i}' \eta_{i}^{-1}}{\sum_{i=1} \eta_{i}^{-1}} \right]$$
 (2)

The Coulomb potential  $V_i$  arising from neighboring atoms  $N_{\text{neig},i}$  is then calculated as:

$$V_i = \sum_{j=1}^{N_{\text{neig},i}} \frac{\operatorname{erf}(\frac{R_{ij}}{\sqrt{2}\gamma_{ij}})q_j}{R_{ij}} f_{\text{cut}}(R_{ij})$$
(3)

where  $f_{\text{cut}}$  is a cutoff function that ensures that the Coulomb potential contributions and its derivatives smoothly decay to zero at distance  $R_c$ . To avoid a costly Ewald summation, the atomic features, charges, and Coulomb potential are concatenated and fed into a gated multi-layer perceptron (MLP) to predict atomic energies. It should be noted that this approach can be replaced by a traditional Ewald summation to model longer range interactions where necessary, albeit incurring a non-linear scaling cost. As will be shown in subsequent sections, we have not found an Ewald summation to be necessary in our comprehensive benchmarks.

As shown in Fig. ??, QET incurs only a marginal increase in inference cost and exhibits scaling comparable to the standard non-charge-informed TensorNet (hereafter "TensorNet"). In contrast, TensorNet combined with the conventional Qeq scheme exhibits prohibitive non-linear scaling, rendering it impractical for simulations of realistic system sizes.

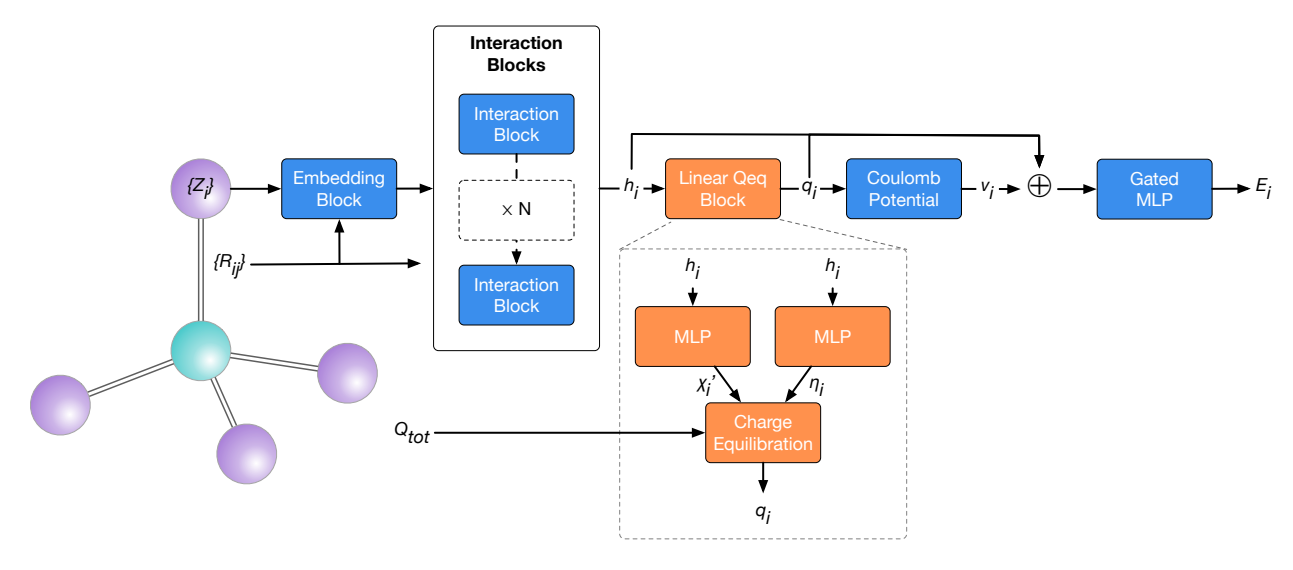


Fig. 1: **QET architecture.** QET takes the atomic number  $Z_i$  and atomic positions  $R_i$  as inputs to an embedding block, which generates a set of rank-2 tensors representing atomic features. These features are subsequently refined through a series of interaction blocks to capture the latent representation of atomic environments. In this work, the cutoff used to define bonds between atoms was set at 5.0 A. The number of interaction blocks and the hidden channel for the embedding, interaction and readout blocks were set to 3 and 64. The graph-convoluted atomic features  $h_i$  and total charge  $Q_{\text{tot}}$  are passed to the LQeq block to compute atomic charges. The LQeq block employs a two-step process to compute atomic charges. First, atomic features are fed into two distinct MLPs to predict environmentdependent electronegativities and hardnesses. To avoid undefined solutions in Eqn. 2, the softplus activation is used to ensure that the predicted hardness values are positive. These quantities are then used to calculate globally distributed charges, constrained by the total charge, using an analytical charge equilibration scheme. The charges are then used to calculate the Coulomb potential  $V_i$  acting on the central atom arising from neighboring atoms. Finally, the atomic features, charges, and Coulomb potential are concatenated and fed into a gated multi-layer perceptron (MLP) to predict atomic energies  $E_i = \phi(h_i \oplus q_i \oplus V_i)$ , which are in turn summed to obtain the total energy.

#### Architecture benchmarks

We benchmark QET using four datasets that have been widely used to evaluate the performance of MLIPs in modeling different charge states and charge transfer in different applications:  $^{11}$  (1) a long carbon chain terminated with hydrogen atoms ( $C_{10}H_2/C_{10}H_3^+$ ); (2) a silver trimer with total charge of  $\pm 1$  ( $Ag_3^{+/-}$ ); (3) an ionized  $Na_9Cl_8^+$  cluster with a removed Na atom; and (4) gold dimer adsorption on MgO(001) surface with and without Al doping. MLIPs that do not incorporate atomic charges struggle to achieve reliable energy and force errors in these systems.

Table 1: Test root mean squared errors (RMSE) of energies, forces, and charges predicted by QET and three charge-informed MLIPs. The reference datasets were obtained from Ref 11, and were generated using FHI-aims<sup>28</sup> with the Perdew-Burke-Ernzerhof (PBE) functional.<sup>29</sup> The 4G-HDNNP and Charge Equilibration Layer for Long-range Interactions (CELLI)<sup>17</sup> models are explicitly trained on energies, forces, and charges, whereas Cartesian Atomic Cluster Expansion with Long-Range (CACE-LR)<sup>20</sup> model learns charges implicitly by being trained only on energies and forces. Values are reported in the order of energies (meV atom<sup>-1</sup>), forces (meV Å<sup>-1</sup>), and charges (me). The lowest errors in each category are bolded.

System	4G-HDNNP	CELLI	CACE-LR	$\operatorname{QET}$
$C_{10}H_2/C_{10}H_3$	1.194/78.00/6.577	0.817/46.54/4.92	0.73/36.90/N.A	<b>0.644</b> / <b>28.527</b> /5.657
$\mathrm{Ag}_3^{+/-}$	1.323/31.69/9.976	1.63/28.71/7.24	<b>0.162</b> /29.0/N.A	7.924/ <b>14.019</b> / <b>1.812</b>
$Na_{8/9}Cl_8^+$	0.481/32.78/15.83	0.412/26.39/15.05	0.21/9.78/N.A	0.575/27.309/ <b>11.521</b>
$Au_2$ - $MgO(001)$	0.219/66.00/5.698	0.132/38.03/ <b>5.505</b>	<b>0.073</b> /7.91/N.A	0.509/ <b>4.581</b> /15.488

The trained QET models compare favorably to three charge-informed MLIPs trained on the same datasets (Table 1). The QET models achieve root mean squared errors (RMSEs) in energies less than 1 meV atom<sup>-1</sup> for all datasets except  $Ag_3^{+/-}$  and RMSEs in forces less than 30 meV Å<sup>-1</sup> across all datasets. It should be noted that both 4G-HDNNP and CELLI suffer from the  $\mathcal{O}(N_{atoms}^3)$  scaling of the traditional Qeq scheme, while CACE-LR still requires a best-case  $\mathcal{O}(N_{atoms}^{1.5})$  calculation of electrostatic interactions using the Ewald method. In contrast, QET scales as  $\mathcal{O}(N_{atoms})$ . A crucial observation is that the charges predicted by the LQeq scheme are comparable to those from the conventional Qeq scheme in 4G-HDNNP and CELLI (CACE-LR does not predict atomic charges), demonstrating that

the LQeq approximation (Eqn. 1) does not result in a loss of accuracy in predicted charges and PES properties.

### Importance of electrostatics

Here, we illustrate that incorporating electrostatics leads to not only quantitative but qualitative differences in the simulated behavior of the model systems.

 $\mathrm{Ag_3}^{+/-}$  relaxed geometries and charges

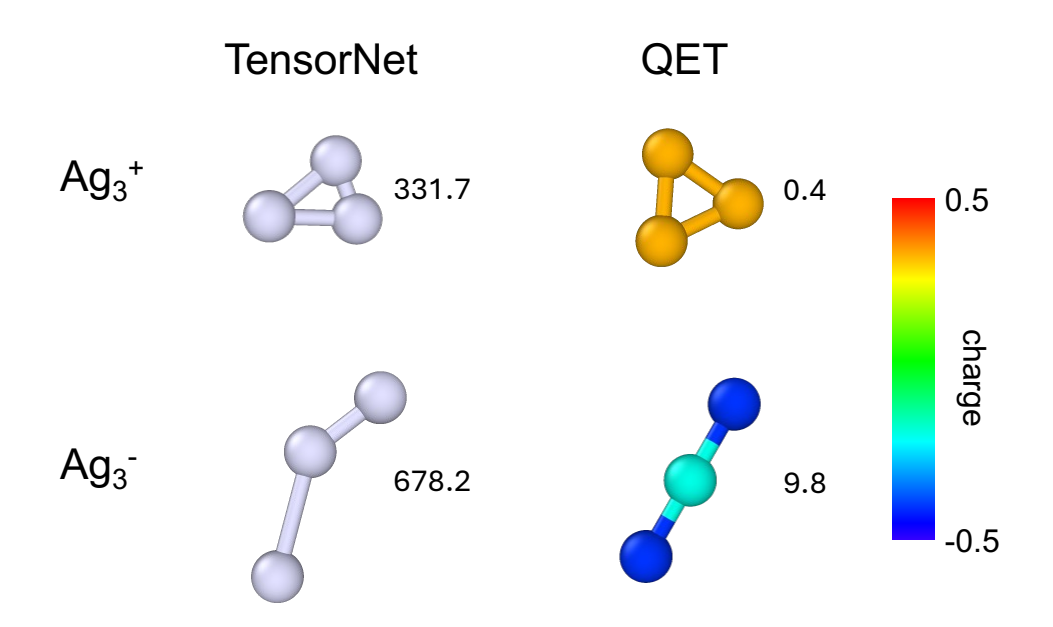


Fig. 2: Relaxed geometry of Ag trimer. Structures of  $Ag_3^+$  and  $Ag_3^-$  optimized using (left) TensorNet and (right) QET. The numbers near each structure indicate the root mean squared structural deviation with respect to the DFT-relaxed structures in units of  $10^{-3}$  Å. The atoms in the QET-relaxed structures are colored based on the QET-predicted partial charges. The structures and charges were visualized using Ovito. <sup>30</sup>

Fig. 2 shows the relaxed geometries of  ${\rm Ag_3}^{+/-}$  using QET and TensorNet. The QET-relaxed structures for  ${\rm Ag_3}^+$  and  ${\rm Ag_3}^-$  have very small root mean square deviations (RMSD) of  $0.4\times 10^{-3}$  Å and  $9.8\times 10^{-3}$  Å, respectively, relative to the DFT-relaxed structures. In contrast, the corresponding RMSDs for the TensorNet-relaxed structures are almost 2 orders of magnitude larger. QET predicts that the energy of  ${\rm Ag_3}^-$  is lower than that of  ${\rm Ag_3}^+$  by -7.864

eV, which is in excellent agreement with the DFT value of -7.865 eV. In contrast, TensorNet predicts a significantly under-estimated energy difference of -0.132 eV. The QET-predicted charges are also within 1 me of the DFT-Hirshfeld charges in both cases.

#### $Au_2$ -MgO(001) energy and force curves

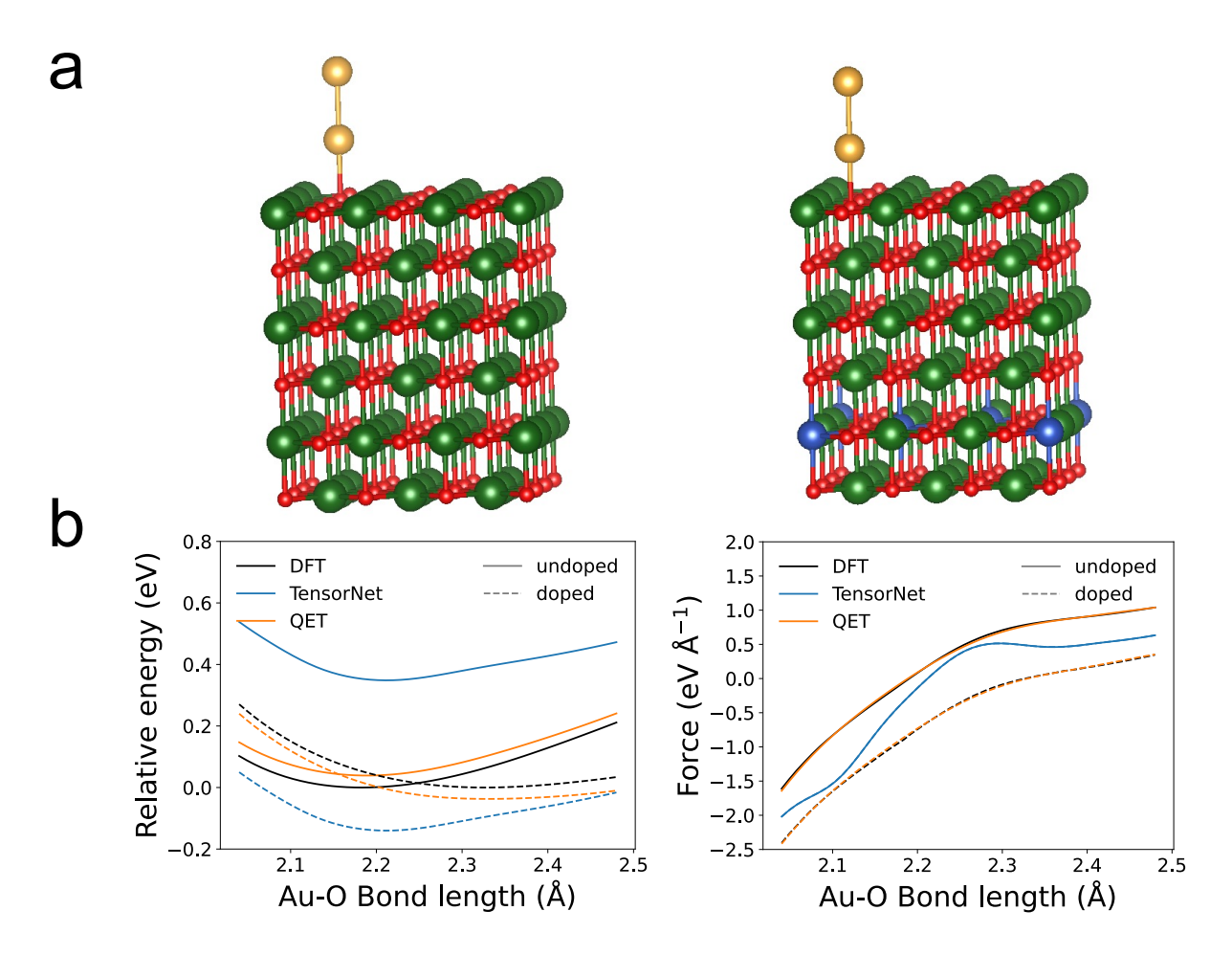


Fig. 3: Charge transfer in an Au dimer on the MgO(001) surface. a The DFT-optimized geometry of the Au dimer on the undoped surface and the Al-doped surface. b Relative (left) energies and (right) forces acting on the Au dimer along the direction perpendicular to the surface for the undoped and Al-doped systems. Predicted energies are referenced to the minimum DFT energy for each case. The Au–O bond length corresponds to the distance between the Au atom nearest to the surface and its neighboring oxygen atom.

Fig. 3 compares the QET, TensorNet and DFT calculated energies as a function of the Au-O bond length in the undoped and doped  $Au_2$ -MgO(001) system. DFT calculations predict two distinct energy and force curves for the undoped and doped cases with respect to the distance between the Au dimer and the nearest oxygen atom. The equilibrium bond length predicted by DFT for the undoped case is approximately 2.19 Å, while that for the Al-doped case is approximately 2.33 Å. The QET energy and forces curves are in excellent agreement with the reference DFT curves, and the equilibrium bond lengths are within 0.01 Å of the DFT values. In contrast, TensorNet predicts the same energy curves with a constant offset and the same force acting on the Au dimer with an equilibrium distance of approximately 2.21 Å for both doped and undoped cases. Additional evidence of the qualitative difference between QET and TensorNet can be seen in the principal component analysis (PCA) of the atomic features (Fig. ??). The TensorNet atomic features fail to distinguish between the undoped and Al-doped cases, while the QET atomic features exhibit two distinct clusters for one of the Au atoms for the undoped and doped surfaces.

## Charge-informed foundation potential

To train a charge-informed QET FP, we generated a Materials Charge (MatQ) dataset, which comprises around 120,000 structures obtained by deforming Materials Project crystals, <sup>31</sup> and rattled relaxation and high-temperature AIMD trajectories in the OMat24<sup>23</sup> validation set. This MatQ data set covers 86 elements and is computed using well-converged DFT static calculations with the Perdew-Burke-Ernzerhof (PBE) functional. <sup>29</sup> The atomic charges are computed with the density derived electrostatic and chemical (DDEC6) electron density partitioning <sup>32</sup> (see Methods section). The distribution of elements, PES properties and charges of the dataset are presented in Figs. ?? and ??.

Fig. ?? shows the parity plots of the PES and charge errors for the QET and TensorNet FPs trained on the MatQ dataset. The test MAEs in energies, forces and stresses of the QET-MatQ FP are 33 meV atoms<sup>-1</sup>, 108 meV Å<sup>-1</sup> and 0.452 GPa, respectively. These MAEs are in line with those of previous state-of-the-art FPs. The MAE of the charges of the QET-MatQ FP is approximately 36.4 me, which is only slightly larger than the MAEs

for the custom QET MLIPs for the model systems in Table 1.

#### Equilibrium and near-equilibrium properties

We benchmarked the QET and TensorNet FP trained using the MatQ dataset (QET-MatQ and TensorNet-MatQ) against three state-of-the-art FPs - TensorNet trained on the MatPES dataset (TensorNet-MatPES-PBE-v2025.1),  $^{22}$  Graph Atomic Cluster Expansion trained on OMat24 and then fine-tuned on the subset of OMat24, Alexandria  $^{33}$  and MPTraj  $^{3}$  (GRACE-2L-OAM)  $^{34}$  and the non-conservative EquiformerV2 trained on OMat24 (EqV2-2L-OMat24-2L).  $^{35}$  We explicitly denote each FP using a "architecture-dataset-version" format. It has been shown that the training dataset has an overwhelming effect on the accuracy of the resulting FP, while the specific architecture plays a relatively minor role.  $^{22}$  All three benchmarked FPs are trained on much larger datasets - MatPES ( $\sim$  400,000 structures) and OMat24/OAM ( $\sim$  100 million structures) - compared to the QET FP (MatQ with  $\sim$  120,000 structures).

From Table. 2, we may observe that the performance of the QET-MatQ FP is in line with our expectations based the training data set. There is a negligible difference in performance between the QET and TensorNet FPs trained on the same MatQ dataset, as well as the TensorNet trained on the MatPES dataset. The slightly better performance of the GRACE-2L-OAM FP is likely due to the much larger size of OMat24 with rattled structures. The non-conservative EqV2-2L-OMat24 only performs well in structure relaxations (d) and heat capacities but significantly worse in mechanical properties.

#### NaCl-CaCl<sub>2</sub> ionic liquid

To illustrate the value of a charge-equilibrated FP, we performed simulations of the well-studied NaCl-CaCl<sub>2</sub><sup>39</sup> ionic liquid system with 1040 atoms using QET-MatQ, TensorNet-MatQ and GRACE-2L-OMat24. We find that the QET-MatQ FP significantly outperforms the TensorNet-MatQ FP in the predicted energies, forces, and stresses of a training set

Table 2: Equilibrium property benchmarks for foundation potentials. Reported values correspond to the average fingerprint distance between the FP-relaxed and DFT-relaxed crystals (d), the mean absolute errors (MAEs) of the bulk modulus  $(K_{\text{vrh}})$ , shear modulus  $(G_{\text{vrh}})$ , and heat capacity  $(C_{\text{v}})$ . The test data for geometry relaxations, elastic and phonon properties were obtained from Ref 36, 37 and 38, respectively, as detailed in Ref. 22.

FP	d	$K_{\rm vrh}$ (GPa)	$G_{\rm vrh}$ (GPa)	$C_{\rm v} ({\rm J~mol^{-1}K^{-1}})$
EqV2-2L-OMat24	0.17	31	22	9
GRACE-2L-OAM	0.23	14	17	7
TensorNet-MatPES	0.37	18	15	29
TensorNet-MatQ	0.37	17	16	18
QET-MatQ	0.35	17	16	17

containing about 800 NaCl-CaCl<sub>2</sub> ionic liquid structures recomputed using consistent DFT settings. The MAEs in energies for QET-MatQ and TensorNet-MatQ are 38 meV atom<sup>-1</sup> and 50 meV atom<sup>-1</sup>, respectively, while the MAEs in forces are 82 and 89 meV Å<sup>-1</sup>, respectively.

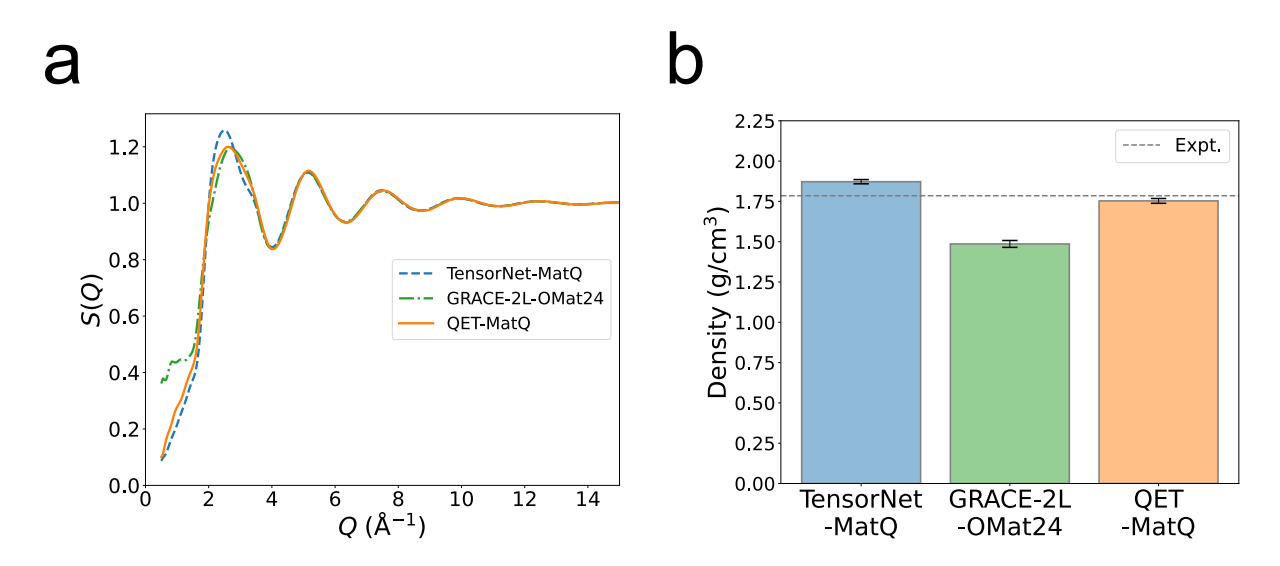


Fig. 4: Simulated structure of NaCl-CaCl<sub>2</sub> ionic liquid. a, Calculated structure factor and b, averaged densities of NaCl-CaCl<sub>2</sub> obtained from 100 ps *NPT* MD simulations at 1200 K using the QET-MatQ, TensorNet-MatQ and GRACE-2L-OMat24 FPs. The experimental density was obtained from Ref. <sup>40,41</sup>

MD simulations using the QET-MatQ, TensorNet-MatQ and GRACE-2L-OMat24 FPs also predict qualitatively different structures for the NaCl-CaCl<sub>2</sub> ionic liquid (Fig. 4a). The structure factors from the QET-MatQ and GRACE-2L-OMat24 simulations agree for Q > 2

Å<sup>-1</sup>. The TensorNet-MatQ FP fails to capture even the same short-range structure, with a significantly higher peak at  $Q = \sim 2.52$  Å<sup>-1</sup>. However, the structure factor from the GRACE-2L-OMat24 simulations deviates significantly from those from the QET-MatQ for Q < 2 Å<sup>-1</sup>. The GRACE-2L-OMat24 simulated structure shows evidence of long-range order (peaks). In contrast, the QET-MatQ structure factor does not exhibit such long-range order, in line with previous computational studies.<sup>39</sup> Furthermore, the average density of the QET-MatQ simulations is in excellent agreement with the experimental density (Fig. 4b), while the TensorNet-MatQ and GRACE-2L-OMat24 simulations significantly overestimate and underestimate the density, respectively.

#### Reactive battery interface simulations

To further demonstrate the utility of QET, we performed simulations of the reactive Li/Li<sub>6</sub>PS<sub>5</sub>Cl interface with fine-tuned QET and TensorNet FPs. The Li/Li<sub>6</sub>PS<sub>5</sub>Cl interface is of major interest in all-solid-state lithium-ion batteries, with an abundance of DFT and experimental data on the reaction products. <sup>42–45</sup> Fine-tuning was carried out on only the PES properties (without charges) using the dataset previously used to fit a custom DeepMD MLIP for this system. <sup>45</sup> The pre-trained QET and TensorNet FPs without fine-tuning do not provide stable simulations of this interface due to the lack of interfacial and surface structures in the training data. The RMSEs of the fine-tuned QET and TensorNet models are provided in Table ??, and are significantly lower than those of the customized DeepMD MLIP. <sup>45</sup>

Fig.5a shows the Li/Li<sub>6</sub>PS<sub>5</sub>Cl interface extracted from 300K MD simulations using the fine-tuned QET-MatQ and TensorNet-MatQ FPs. In the QET simulations, the phosphorus atoms exhibit a wide range of charge values, consistent with their corresponding oxidation states as a  $P^{3-}$  anion or as a  $PS_4^{3-}$  polyanion. The sulfur and chlorine atoms are consistently negatively charged, while the lithium atoms are either nearly neutral or positively charged. The P-P radial distribution function (RDF) is shown in Fig.5b and those for Li-X (X = P, S, Cl) are provided in Fig.??. Most of the peaks in the RDFs can be attributed

to the formation of known interfacial reaction products such as Li<sub>3</sub>P, Li<sub>2</sub>S, LiCl, etc. In TensorNet simulations, a short P–P bond of 2.2 Å is observed after approximately 1 ns, which corresponds to the length of the P-P bond in elemental phosphorus. The formation of elemental phosphorus has never been observed in previous DFT or experimental studies, <sup>46</sup> and we speculate that this is the result of the lack of charge interactions in the TensorNet simulations. No such elemental P-P bonds were observed in the QET simulations. A PCA analysis of the Li latent features in the QET simulations (Fig. ??) finds that distinct clusters corresponding to different local environments, e.g., in bcc Li metal, in bulk Li<sub>6</sub>PS<sub>5</sub>Cl and experimentally known reaction products such as Li<sub>3</sub>P, Li<sub>2</sub>S and LiCl at the interface.

We next demonstrate QET's ability to simulate reactions under an external potential. Anodic and cathodic biases were imposed by shifting the electronegativities of Li atoms in the top three electrode layers to mimic applied potentials of +4 V and -4 V, respectively. As shown in Fig.5c, a cathodic bias (-4 V) accelerates interfacial reactions; the interphase thickens continuously and the potential energy decreases over the entire trajectory. In contrast, an anodic bias (+4 V) suppresses reactions; the interphase thickness plateaus and the potential energy becomes stationary after  $\sim 0.2$  ns. Charge maps (Fig.5d) further corroborate the bias response, with the -4 V bias scenario exhibiting greater structural and charge disorder, and a greater spread of partial charges across the interphase. The RDF analysis (Fig. 6) also shows significantly higher peak intensities corresponding to interfacial reaction products such as  $\text{Li}_3\text{P}$ ,  $\text{Li}_2\text{S}$ , and LiCl, and a lower peak intensities corresponding to  $\text{Li}_6\text{PS}_5\text{Cl}$ , under an applied potential of -4 V compared to +4 V. Together, these results show that QET can accurately capture voltage-dependent interfacial chemistry in large-scale MD simulations.

## Discussion

Incorporating electrostatic interactions is a crucial next step in the evolution of FPs. Here we demonstrate two key advances: a linear-scaling, charge-aware QET architecture and the

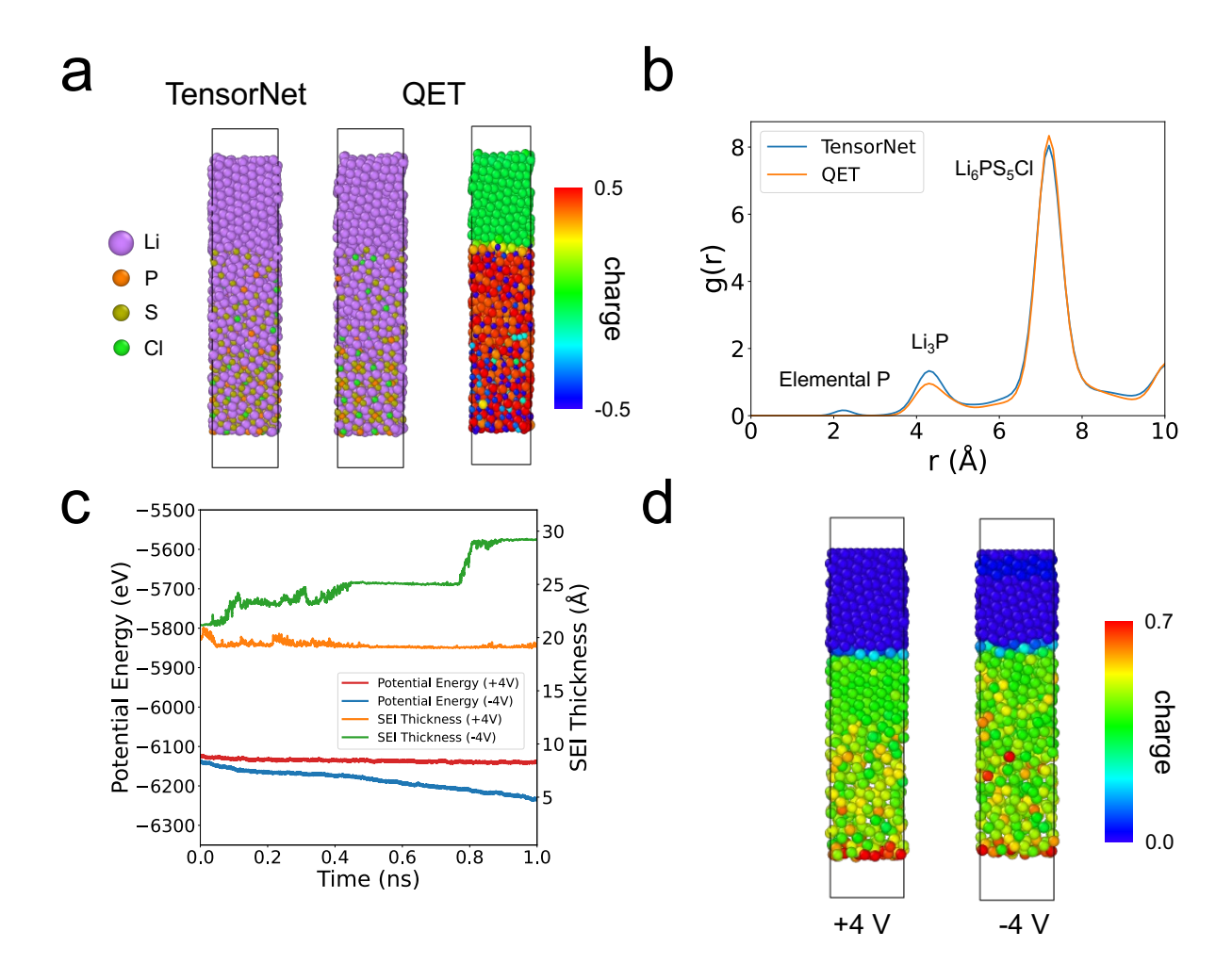


Fig. 5: Reactive simulations of the  $\text{Li}/\text{Li}_6\text{PS}_5\text{Cl}$  interface. a, Snapshots of the solid electrolyte interphase at t=1.1 ns from NVT MD simulations performed using fine-tuned QET and TensorNet potentials. b, Radial distribution function, calculated from the last 1 ns of the trajectory. c, Potential energy and interphase thickness of the  $\text{Li}/\text{Li}_6\text{PSCl}_5$  interphase obtained from the last 1 ns under applied potentials of +4 V and -4 V. d, Comparison of the charge distribution on Li atoms at t=1.1 ns for applied potentials of +4 V and -4 V. All visualizations were performed using Ovito. The heatmap colors indicate the partial charges predicted by QET.

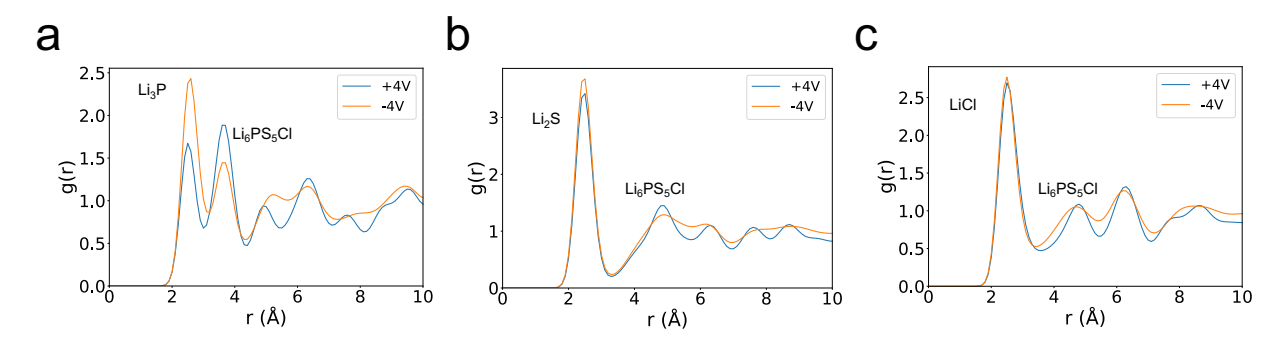


Fig. 6: Local environment of Li atoms in  $\text{Li/Li}_6\text{PSCl}_5$  under an applied potential. Calculated radial distribution functions of a Li-P, b Li-S and c Li-Cl pairs from the last 1 ns of NVT MD simulations under applied potentials of +4 V and -4 V.

training of a QET FP on a large, charge-informed dataset (MatQ).

A linear-scaling charge-equilibration scheme is essential for FPs to transcend conventional limits of length and time scales. For a 1-million-atom polycrystalline model, the LQeq method is estimated to be 21 orders of magnitude faster than the traditional Qeq scheme, assuming similar prefactors. This effectively removes the long-standing electrostatic bottleneck in large-scale reactive simulations.

Charge-aware FPs open a pathway to model phenomena governed by charge transfer. QET produces qualitatively distinct predictions across multiple benchmark systems and accurately captures the structure of the NaCl–CaCl<sub>2</sub> ionic liquid. The approach is particularly powerful for modeling reactive interfaces, such as electrode–electrolyte interfaces in batteries and adsorbate–catalyst interactions in heterogeneous catalysis, where charge redistribution drives functionality. Moreover, QET enables simulations under applied electrochemical potentials.

This work provides a proof of concept that an FP can be simultaneously accurate, reactive, and scalable. Further improvements in accuracy will come from expanding the diversity and fidelity of training data through broader community datasets such as MatPES<sup>22</sup> or targeted fine-tuning for specific chemistries. Continued advances in architecture and algorithms will enhance parameter efficiency and inference speed. We urge the community to include atomic charges and magnetic moments in future open datasets, as such information is essen-

tial for developing more physically grounded FPs. With these collective efforts, charge-aware FPs like QET can unlock transformative advances across broad materials domains, including energy storage, catalysis, and beyond.

## Methods

#### Dataset construction

The MatQ dataset comprises near-equilibrium and out-of-equilibrium structures. The 6,652,874 near-equilibrium structures comprise Materials Project crystals subject to strains of  $\pm 2\%$ ,  $\pm 4\%$  and  $\pm 6\%$  along all crystallographic directions. The out-of-equilibrium structures were obtained from the OMat24 validation set of 1,025,361 structures. The DImensionality-Reduced Encoded Clusters with sTratified (DIRECT) sampling approach 47 was then used to select 60,000 structures each from the near-equilibrium and out-of-equilibrium sets that comprehensively covers the configuration space with minimal overlap, significantly reducing the computational cost of reference data generation.

Spin-polarized static DFT calculations were then performed using the Vienna Ab initio Simulation Package (VASP). <sup>48</sup> The generalized gradient approximation (GGA) Perdew-Burke-Ernzerhof (PBE) <sup>29</sup> functional was employed to describe exchange-correlation interactions. The input files were generated using the "MatPESStaticSet" input set implemented in the Python Materials Genomics (pymatgen) package, <sup>49</sup> which has been carefully benchmarked to ensure well-converged PES properties. <sup>22</sup> The main parameters include a plane-wave kinetic energy cutoff of 680 eV, a k-spacing of 0.35 Å<sup>-1</sup>, and an electronic convergence condition of  $10^{-5}$  eV. DDEC6 charges were computed using chargemol (version:  $09_{-26_{-2}017})^{50}$  from the DFT charge densities.

The final MatQ dataset contains 114,445 structures, after excluding unconverged DFT calculations and structures with extremely large force components ( $|F_{x,y,z}| > 50$  eV Å<sup>-1</sup>). The fine-tuning dataset for Li/Li<sub>6</sub>PS<sub>5</sub>Cl was obtained from Ref. 45.

#### Model training

The datasets were split into 90% for training and 10% for validation. All model training was conducted using PyTorch Lightning. The AMSGrad variant of the AdamW optimizer was selected with a learning rate of  $10^{-3}$  and a weight decay coefficient of  $10^{-5}$ . A cosine annealing scheduler adjusted the learning rate during training, with a maximum of  $10^4$  iterations and a minimum learning rate of  $10^{-5}$ . The loss function for potential training is defined as:

$$\mathcal{L}_{total} = w_E \mathcal{L}(E^{\text{MLIP}}, E^{\text{DFT}}) + w_F \mathcal{L}(F^{\text{MLIP}}, F^{\text{DFT}}) + w_\sigma \mathcal{L}(\sigma^{\text{MLIP}}, \sigma^{\text{DFT}}) + w_q \mathcal{L}(q^{\text{MLIP}}, q^{\text{DFT}}),$$
(4)

where E, F,  $\sigma$ , and q represent the total energy per atom, force components, stress tensor, and partial charge, respectively, and L is the Huber loss function with default PyTorch settings in this work.

For training the custom potentials for the four model systems, only charges, energies and forces were included in the loss function with weights  $w_E = 1.0$ ,  $w_F = 1.0$  and  $w_q = 0.1$  ( $w_{\sigma} = 0$ ). For training the FPs, the weights used were  $w_E = 1.0$ ,  $w_F = 1.0$ ,  $w_{\sigma} = 0.1$ ,  $w_q = 1.0$ . For fine-tuning on the Li/Li<sub>6</sub>PS<sub>5</sub>Cl dataset without reference charges,  $w_q$  was set to 0 to minimize the error of PES properties with respect to DFT calculations.

The number of training epochs was set at 1,000 and 250 for model training and fine-tuning, respectively. Early stopping was triggered when the validation loss did not decrease for 500 epochs for model training and for 50 epochs for fine-tuning. A batch size of 8 was used to train customized potentials, while a larger batch size of 32 was used for FP training. A smaller batch size of 8 was used for fine-tuning to accommodate the much larger system sizes in the dataset.

To reduce the range of target energies and improve convergence, we subtracted the total energies by the weighted sum of their elemental reference energies to arrive at a cohesive energy. These elemental reference energies,  $\mathbf{E}_{\text{elem}}$ , were determined through linear regression

according to

$$\mathbf{E}_{\text{elem}} = (\mathbf{A}^T \mathbf{A})^{-1} \mathbf{A}^T \mathbf{E}_{\text{total}},\tag{5}$$

where  $\mathbf{E}_{\text{total}}$  denotes the vector of total energies,  $N_{\text{struct}}$  is the total number of structures in the dataset,  $N_{\text{elem}}$  is the number of distinct chemical elements, and  $\mathbf{A}$  is the composition matrix constructed by stacking  $\mathbf{n}_{\text{elem}}$ , the counts of each element per structure, across all structures. The total energy from the atomic energies can be recovered using the following expression:

$$E_{total} = \sum_{i}^{N_{\text{atom}}} \sigma E_i + \mathbf{n_{elem}} \cdot \mathbf{E}_{elem}$$
 (6)

where the scaling factor  $\sigma$  is the root mean square of all atomic force components in the training set.

#### **MD Simulations**

All molecular dynamics (MD) simulations were performed using the Atomic Simulation Environment (ASE)<sup>51</sup> package (version 3.25.0). The time step was set to 1 fs. The Nosé-Hoover thermostat, combined with the isotropic Martyna-Tobias-Klein (MTK) barostat with a temperature damping parameter of  $T_{\rm damp} = 100$  fs and a pressure damping parameter of  $P_{\rm damp} = 1000$  fs, was used in the NpT MD simulations. The Langevin thermostat with a very small friction coefficient of  $\gamma = 0.001$  ps<sup>-1</sup> was applied to perform NVT simulations to accurately capture the dynamics of atoms in the solid electrolyte interphase.

## Benchmarking details

For the geometry relaxation of  $Ag_3^{+/-}$ , each atom in the DFT structures was randomly displaced between -1.0 and 1.0 Å, and the system was then relaxed using the Broyden–Fletcher–Goldfarb–Shan (BFGS) algorithm to the nearest local minimum until the maximum force was below 0.01 eV Å<sup>-1</sup>. The PES analysis of the Au dimer in undoped and Al-doped MgO was conducted by performing 50 single-point calculations at evenly spaced intervals from 2.04 Å to 2.48 Å.

The equilibrium and near-equilibrium FP benchmarks including fingerprint distance, elasticity, heat capacity were performed using MatCalc<sup>52</sup> and detailed in Ref. 22. The NaCl-CaCl<sub>2</sub> ionic liquid test data was obtained from Ref. 39 and recomputed with the same DFT settings as the training set for the FPs.

The total structure factor of the ionic liquid was computed based on the partial pair distribution functions  $g_{ij}(r)$  obtained from MD simulations. The partial structure factors  $S_{ij}(Q)$  were calculated using the Faber–Ziman formalism:

$$S_{ij}(Q) - 1 = \rho \int_0^\infty 4\pi r^2 \left[ g_{ij}(r) - 1 \right] \frac{\sin(Qr)}{Qr} dr,$$
 (7)

where  $\rho$  is the number density, Q is the magnitude of the scattering vector, and r is the interatomic distance.

The total X-ray weighted structure factor  $S_X(Q)$  was then obtained as

$$S_X(Q) = \sum_{i} \sum_{j \ge i} c_i c_j f_i(Q) f_j(Q) \left[ S_{ij}(Q) - 1 \right], \tag{8}$$

where  $c_i$  and  $f_i(Q)$  denote the atomic concentration and X-ray scattering factor of species i, respectively.

Finally, the normalized total structure factor was expressed as

$$S(Q) = 1 + \frac{S_X(Q)}{\left[\sum_i c_i f_i(Q)\right]^2}.$$
(9)

The atomic form factors f(s) were evaluated using the standard analytical expression

$$f(s) = Z - 41.78214 s^{2} \sum_{n=1}^{4} a_{n} \exp(-b_{n}s^{2}), \tag{10}$$

where Z is the atomic number,  $s = \sin(\theta)/\lambda$ , and  $a_n$  and  $b_n$  are element-specific coefficients taken from the *International Tables for Crystallography*.

The radial distribution functions of the SEI for the Li/Li<sub>6</sub>PS<sub>5</sub>Cl system were calculated from the last 100 ps of the MD trajectory using the pymatgen-analysis-diffusion package. <sup>42</sup> A cutoff of 3 Å was set to determine the nearest neighbors of all Li atoms. For the composition profile along the z-axis of the simulation cell, we divided the effective simulation cell (excluding the vacuum region) into 40 bins of equal width. The fraction of lithium  $f_{i,\text{Li}}$  in each bin is then calculated as follows:

$$f_{i,\text{Li}} = \frac{N_{\text{Li}}}{N_{i,\text{total}}},\tag{11}$$

where  $N_{i,\text{total}}$  denotes the total number of atoms in the volume of bin i. A Gaussian smoothening with  $\sigma = 1.5$  Å was applied. The phase classification criteria were defined as follows:

Table 3: Phase classification criteria for  ${\rm Li/Li_6PS_5Cl}$  interface simulations.

Phase	Criteria
bulk bcc Li	$f_{\rm Li} > 0.9$
interface	$0.5 \le f_{\rm Li} \le 0.9$
$\mathrm{Li_6PS_5Cl}$	$f_{\rm Li} < 0.5$

The SEI thickness was calculated for each frame of the trajectory at 10 fs intervals, and a rolling average over 200 frames (2 ps) was applied to clearly visualize trends while minimizing fluctuations.

# Acknowledgement

This work was intellectually led by the U.S. Department of Energy, Office of Science, Office of Basic Energy Sciences, Materials Sciences and Engineering Division under contract No. DE-AC02-05-CH11231 (Materials Project program KC23MP). The Li/Li<sub>6</sub>PS<sub>5</sub>Cl interface benchmarking work was supported by the Energy Storage Research Alliance (DE-AC02-06CH11357), an Energy Innovation Hub funded by the US Department of Energy, Office

of Science, Basic Energy Sciences. This research used resources from the National Energy Research Scientific Computing Center (NERSC), a Department of Energy Office of Science User Facility under NERSC award DOE-ERCAP0026371. T. W. Ko also acknowledges the support of the Eric and Wendy Schmidt AI in Science Postdoctoral Fellowship, a Schmidt Futures program.

## Data Availability

The 4G-HDNNP datasets are available at https://archive.materialscloud.org/record/2020.137. The Li/Li<sub>6</sub>PS<sub>5</sub>Cl dataset is available at https://aissquare.com/datasets/detail?pageType=datasets&name=Training\_data&id=347.

## Code Availability

The QET architecture is implemented in the open-source Materials Graph Library (MatGL) package. The DIRECT sampling algorithm is implemented in the Materials Machine Learning (maml) package (https://github.com/materialsvirtuallab/maml), and the FP benchmarks were performed using the MatCalc package (https://github.com/materialsvirtuallab/matcalc).

## Author contributions

T.W.K. and S.P.O. conceived the idea and designed the study. T.W.K. proposed and implemented the QET architectures and supervised the project from data generation to the design of benchmarks. R.L. led the benchmarking for FPs, while A.R.M. led the benchmarking for fine-tuning MLIPs and conducted dimensionality reduction analyses. R.L., Z.Y., and J.Q. contributed to data sampling and generation. T.W.K. and S.P.O. prepared the initial draft, and all authors contributed to the discussion and revision.

## Completing Interests

A provisional patent application has been filed covering aspects of the QET architecture and training.

# References

- (1) Ko, T. W.; Ong, S. P. Recent advances and outstanding challenges for machine learning interatomic potentials. *Nat. Comput. Sci.* **2023**, 1–3.
- (2) Chen, C.; Ong, S. P. A universal graph deep learning interatomic potential for the periodic table. *Nat. Comput. Sci.* **2022**, *2*, 718–728.
- (3) Deng, B.; Zhong, P.; Jun, K.; Riebesell, J.; Han, K.; Bartel, C. J.; Ceder, G. CHGNet as a pretrained universal neural network potential for charge-informed atomistic modelling. *Nat. Mach. Intell.* **2023**, *5*, 1031–1041.
- (4) Batatia, I.; Kovacs, D. P.; Simm, G.; Ortner, C.; Csányi, G. MACE: Higher order equivariant message passing neural networks for fast and accurate force fields. Adv. Neural Inf. Process. Syst. 2022, 35, 11423–11436.
- (5) Batzner, S.; Musaelian, A.; Sun, L.; Geiger, M.; Mailoa, J. P.; Kornbluth, M.; Molinari, N.; Smidt, T. E.; Kozinsky, B. E (3)-equivariant graph neural networks for dataefficient and accurate interatomic potentials. *Nat. Commun.* **2022**, *13*, 2453.
- (6) Lysogorskiy, Y.; Bochkarev, A.; Drautz, R. Graph atomic cluster expansion for foundational machine learning interatomic potentials. arXiv preprint arXiv:2508.17936 2025,
- (7) Giraldo, J. H.; Skianis, K.; Bouwmans, T.; Malliaros, F. D. On the trade-off between over-smoothing and over-squashing in deep graph neural networks. Proceedings of the 32nd ACM international conference on information and knowledge management. 2023; pp 566–576.

- (8) Rappe, A. K.; Goddard III, W. A. Charge equilibration for molecular dynamics simulations. *J. Phys. Chem.* **1991**, *95*, 3358–3363.
- (9) Ko, T. W.; Finkler, J. A.; Goedecker, S.; Behler, J. General-purpose machine learning potentials capturing nonlocal charge transfer. *Acc. Chem. Res.* **2021**, *54*, 808–817.
- (10) Kocer, E.; Ko, T. W.; Behler, J. Neural network potentials: A concise overview of methods. *Ann. Rev. Phys. Chem.* **2022**, *73*, 163–186.
- (11) Ko, T. W.; Finkler, J. A.; Goedecker, S.; Behler, J. A fourth-generation high-dimensional neural network potential with accurate electrostatics including non-local charge transfer. *Nat. Commun.* 2021, 12, 398.
- (12) Ko, T. W.; Finkler, J. A.; Goedecker, S.; Behler, J. Accurate Fourth-Generation Machine Learning Potentials by Electrostatic Embedding. J. Chem. Theory Comput. 2023,
- (13) Anstine, D. M.; Zubatyuk, R.; Isayev, O. AIMNet2: a neural network potential to meet your neutral, charged, organic, and elemental-organic needs. *Chem. Sci.* 2025, 16, 10228–10244.
- (14) Ghasemi, S. A.; Hofstetter, A.; Saha, S.; Goedecker, S. Interatomic potentials for ionic systems with density functional accuracy based on charge densities obtained by a neural network. *Phys. Rev. B* **2015**, *92*, 045131.
- (15) Jacobson, L. D.; Stevenson, J. M.; Ramezanghorbani, F.; Ghoreishi, D.; Leswing, K.; Harder, E. D.; Abel, R. Transferable neural network potential energy surfaces for closed-shell organic molecules: Extension to ions. J. Chem. Theory Comput. 2022, 18, 2354–2366.
- (16) Maruf, M. U.; Kim, S.; Ahmad, Z. Equivariant Machine Learning Interatomic Potentials with Global Charge Redistribution. arXiv preprint arXiv:2503.17949 2025,

- (17) Fuchs, P.; Sanocki, M.; Zavadlav, J. Learning Non-Local Molecular Interactions via Equivariant Local Representations and Charge Equilibration. arXiv preprint arXiv:2501.19179 2025,
- (18) Frank, J. T.; Chmiela, S.; MÞller, K.-R.; Unke, O. T. Euclidean fast attention: Machine learning global atomic representations at linear cost. arXiv preprint arXiv:2412.08541 2024,
- (19) Yue, S.; Muniz, M. C.; Calegari Andrade, M. F.; Zhang, L.; Car, R.; Panagiotopoulos, A. Z. When do short-range atomistic machine-learning models fall short? *J. Chem. Phys.* **2021**, *154*.
- (20) Kim, D.; King, D. S.; Zhong, P.; Cheng, B. Learning charges and long-range interactions from energies and forces. arXiv preprint arXiv:2412.15455 2024,
- (21) Wang, Y.; Cheng, C.; Li, S.; Ren, Y.; Shao, B.; Liu, G.; Heng, P.-A.; Zheng, N. Neural P<sup>3</sup> M: A Long-Range Interaction Modeling Enhancer for Geometric GNNs. *Adv. Neural Inf. Process. Syst.* **2024**, *37*, 120336–120365.
- (22) Kaplan, A. D.; Liu, R.; Qi, J.; Ko, T. W.; Deng, B.; Riebesell, J.; Ceder, G.; Persson, K. A.; Ong, S. P. A foundational potential energy surface dataset for materials. arXiv preprint arXiv:2503.04070 2025,
- (23) Barroso-Luque, L.; Shuaibi, M.; Fu, X.; Wood, B. M.; Dzamba, M.; Gao, M.; Rizvi, A.; Zitnick, C. L.; Ulissi, Z. W. Open materials 2024 (omat24) inorganic materials dataset and models. arXiv preprint arXiv:2410.12771 2024,
- (24) Simeon, G.; De Fabritiis, G. Tensornet: Cartesian tensor representations for efficient learning of molecular potentials. *Adv. Neural Inf. Process. Syst.* **2023**, *36*, 37334–37353.
- (25) Liao, Y.-L.; Wood, B.; Das\*, A.; Smidt\*, T. EquiformerV2: Improved Equivariant

- Transformer for Scaling to Higher-Degree Representations. International Conference on Learning Representations (ICLR). 2024.
- (26) Essmann, U.; Perera, L.; Berkowitz, M. L.; Darden, T.; Lee, H.; Pedersen, L. G. A smooth particle mesh Ewald method. J. Chem. Phys. 1995, 103, 8577–8593.
- (27) Wang, Y.; Pulido, I.; Takaba, K.; Kaminow, B.; Scheen, J.; Wang, L.; Chodera, J. D. Espalomacharge: Machine learning-enabled ultrafast partial charge assignment. *J. Phys. Chem. A* **2024**, *128*, 4160–4167.
- (28) Blum, V.; Gehrke, R.; Hanke, F.; Havu, P.; Havu, V.; Ren, X.; Reuter, K.; Scheffler, M. Ab initio molecular simulations with numeric atom-centered orbitals. Comput. Phys. Commun. 2009, 180, 2175–2196.
- (29) Perdew, J. P.; Burke, K.; Ernzerhof, M. Generalized gradient approximation made simple. *Phys. Rev. Lett.* **1996**, *77*, 3865.
- (30) Stukowski, A. Visualization and analysis of atomistic simulation data with OVITO-the Open Visualization Tool. *Model. Simul. Mat. Sci. Eng.* **2009**, *18*, 015012.
- (31) Horton, M. K.; Huck, P.; Yang, R. X.; Munro, J. M.; Dwaraknath, S.; Ganose, A. M.; Kingsbury, R. S.; Wen, M.; Shen, J. X.; Mathis, T. S.; others Accelerated data-driven materials science with the Materials Project. *Nat. Mat.* **2025**, 1–11.
- (32) Manz, T. A.; Limas, N. G. Introducing DDEC6 atomic population analysis: part 1. Charge partitioning theory and methodology. RSC Adv. 2016, 6, 47771–47801.
- (33) Schmidt, J.; Cerqueira, T. F.; Romero, A. H.; Loew, A.; Jäger, F.; Wang, H.-C.; Botti, S.; Marques, M. A. Improving machine-learning models in materials science through large datasets. *Mater. Today Phys.* **2024**, *48*, 101560.
- (34) Bochkarev, A.; Lysogorskiy, Y.; Drautz, R. Graph atomic cluster expansion for semilocal interactions beyond equivariant message passing. *Phys. Rev. X* **2024**, *14*, 021036.

- (35) Liao, Y.-L.; Wood, B. M.; Das, A.; Smidt, T. EquiformerV2: Improved Equivariant Transformer for Scaling to Higher-Degree Representations. The Twelfth International Conference on Learning Representations. 2024.
- (36) Wang, H.-C.; Botti, S.; Marques, M. A. L. Predicting stable crystalline compounds using chemical similarity. *npj Comput. Mater.* **2021**, *7*, 1–9.
- (37) Dunn, A.; Wang, Q.; Ganose, A.; Dopp, D.; Jain, A. Benchmarking materials property prediction methods: the Matbench test set and Automatminer reference algorithm. *npj* Comput. Mater. **2020**, *6*, 138.
- (38) Loew, A.; Sun, D.; Wang, H.-C.; Botti, S.; Marques, M. A. Universal machine learning interatomic potentials are ready for phonons. *npj Computational Materials* **2025**, *11*, 178.
- (39) Guo, J.; Woo, V.; Andersson, D. A.; Hoyt, N.; Williamson, M.; Foster, I.; Benmore, C.; Jackson, N. E.; Sivaraman, G. AL4GAP: Active learning workflow for generating DFT-SCAN accurate machine-learning potentials for combinatorial molten salt mixtures. *J. Chem. Phys.* **2023**, *159*.
- (40) Janz, G. J. Thermodynamic and transport properties for molten salts: correlation equations for critically evaluated density, surface tension, electrical conductance, and viscosity data. J. phys. chem. ref. data 1988, 17.
- (41) Janz, G. J.; Allen, C. B.; Bansal, N.; Murphy, R.; Tomkins, R. Physical properties data compilations relevant to energy storage. II. Molten salts: data on single and multi-component salt systems; 1979.
- (42) Deng, Z.; Zhu, Z.; Chu, I.-H.; Ong, S. P. Data-driven first-principles methods for the study and design of alkali superionic conductors. *Chem. Mater.* **2017**, *29*, 281–288.

- (43) Xu, H.; Cao, G.; Shen, Y.; Yu, Y.; Hu, J.; Wang, Z.; Shao, G. Enabling Argyrodite Sulfides as Superb Solid-State Electrolyte with Remarkable Interfacial Stability Against Electrodes. *Energy Environ. Mater.* **2022**, *5*, 852–864.
- (44) Chen, Y.; Gao, X.; Zhen, Z.; Chen, X.; Huang, L.; Zhou, D.; Hu, T.; Ren, B.; Xu, R.; Chen, J.; others The construction of multifunctional solid electrolyte interlayers for stabilizing Li 6 PS 5 Cl-based all-solid-state lithium metal batteries. *Energy Environ. Sci.* 2024, 17, 9288–9302.
- (45) An, Y.; Hu, T.; Pang, Q.; Xu, S. Observing Li Nucleation at the Li Metal–Solid Electrolyte Interface in All-Solid-State Batteries. *ACS nano* **2025**, *19*, 14262–14271.
- (46) Chen, M.; Ko, H.-Y.; Remsing, R. C.; Calegari Andrade, M. F.; Santra, B.; Sun, Z.; Selloni, A.; Car, R.; Klein, M. L.; Perdew, J. P.; others Ab initio theory and modeling of water. *Proc. Natl. Acad. Sci.* 2017, 114, 10846–10851.
- (47) Qi, J.; Ko, T. W.; Wood, B. C.; Pham, T. A.; Ong, S. P. Robust training of machine learning interatomic potentials with dimensionality reduction and stratified sampling. npj Comput. Mater. 2024, 10, 43.
- (48) Kresse, G.; Furthmüller, J. Efficient iterative schemes for ab initio total-energy calculations using a plane-wave basis set. *Phy. Rev. B* **1996**, *54*, 11169.
- (49) Ong, S. P.; Richards, W. D.; Jain, A.; Hautier, G.; Kocher, M.; Cholia, S.; Gunter, D.; Chevrier, V. L.; Persson, K. A.; Ceder, G. Python Materials Genomics (pymatgen): A robust, open-source python library for materials analysis. *Comput. Mater. Sci.* 2013, 68, 314–319.
- (50) Limas, N. G.; Manz, T. A. Introducing DDEC6 atomic population analysis: part 4. Efficient parallel computation of net atomic charges, atomic spin moments, bond orders, and more. RSC Adv. 2018, 8, 2678–2707.

- (51) Larsen, A. H.; Mortensen, J. J.; Blomqvist, J.; Castelli, I. E.; Christensen, R.; Dułak, M.; Friis, J.; Groves, M. N.; Hammer, B.; Hargus, C.; others The atomic simulation environment—a Python library for working with atoms. *J. Condens. Matter Phys.* **2017**, *29*, 273002.
- (52) Liu, R.; Liu, E.; Riebesell, J.; Qi, J.; Ko, T. W.; Ong, S. P. MatCalc. 2024; https://github.com/materialsvirtuallab/matcalc.

# SUPPLEMENTARY INFORMATION

# A Fast, Accurate, and Reactive Equivariant Foundation Potential

Tsz Wai Ko,\* Runze Liu, Adesh Rohan Mishra, Zihan Yu, Ji Qi, and Shyue Ping Ong\*

Aiiso Yufeng Li Family Department of Chemical and Nano Engineering, University of California San Diego, 9500 Gilman Dr, Mail Code 0448, La Jolla, CA 92093-0448, United States

E-mail: t1ko@ucsd.edu; ongsp@ucsd.edu

## Charge equilibration scheme

The charge equilibration (Qeq) scheme determines the global charge distribution by minimizing the following energy expression:

$$E_{Qeq} = \sum_{i=1}^{N_{\text{atoms}}} (\chi_i q_i + \frac{1}{2} \eta_i q_i^2) + E_{\text{elec}}$$
 (1)

with respect to the charges, where  $\chi_i$  and  $\eta_i$  denotes the atomic electronegativities and hardnesses. The electrostatic energy is computed using a set of Gaussian distributed charges according to Coulomb's law:

$$E_{\text{elec}} = \sum_{i=1}^{N_{\text{atoms}}} \sum_{j < i}^{N_{\text{atoms}}} \frac{\operatorname{erf}\left(\frac{R_{ij}}{\sqrt{2\gamma_{ij}}}\right)}{R_{ij}} q_i q_j + \sum_{i=1}^{N_{\text{atoms}}} \frac{q_i^2}{2\sigma_i \sqrt{\pi}}$$
(2)

with

$$\gamma_{ij} = \sqrt{\sigma_i^2 + \sigma_j^2} \tag{3}$$

and the  $\sigma_i$  representing the widths of the Gaussian charge densities. The energy minimization yields a set of linear equations

$$\frac{\partial E_{\text{Qeq}}}{\partial q_i} = 0, \forall i = 1, ..., N_{\text{atoms}} \implies \sum_{j=1}^{N_{\text{atoms}}} A_{ij} q_j + \chi_i = 0$$
(4)

, where the elements  $\mathbf{A}_{ij}$  are given by

$$A_{ij} = \begin{cases} J_i + \frac{1}{\sigma_i \sqrt{\pi}}, & \text{if } i = j\\ \frac{\text{erf}\left(\frac{R_{ij}}{\sqrt{2}\gamma_{ij}}\right)}{R_{ij}}, & \text{otherwise} \end{cases}$$
 (5)

Adding the constraint that the total charge of the system,  $Q_{\text{tot}}$ , is equal to the sum of the atomic charges via a Lagrange multiplier leads to a modified set of linear equations.

$$\begin{pmatrix}
\mathbf{A} & \vdots \\
 & 1 \\
\hline
1 & \dots & 1 & 0
\end{pmatrix}
\begin{pmatrix}
q_1 \\
\vdots \\
q_{N_{\text{atoms}}} \\
\lambda
\end{pmatrix} = \begin{pmatrix}
-\chi_1 \\
\vdots \\
-\chi_{N_{\text{atoms}}} \\
Q_{\text{tot}}
\end{pmatrix} .$$
(6)

The charges are then determined by solving the  $N_{\text{atoms}+1} \times N_{\text{atoms}+1}$  linear equations.

## Inference time benchmarks

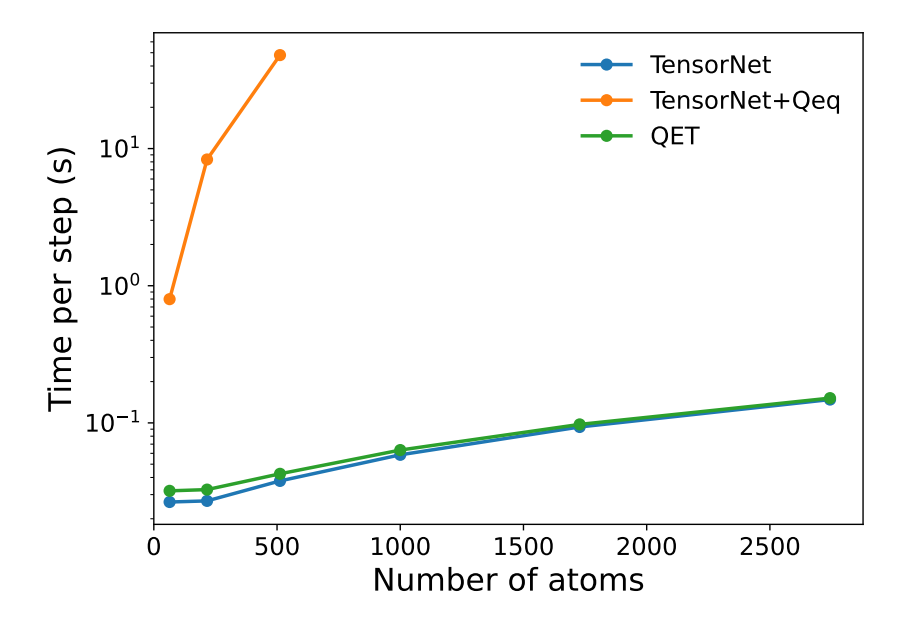


Fig. S1: **Inference time comparison.** The average runtime for 100 single-point calculations of a silicon diamond structure was evaluated for TensorNet, TensorNet with conventional Qeq (TensorNet+Qeq), and QET using supercells containing 64 to 2744 atoms. All calculations were performed on a single NVIDIA RTX 3090 GPU.

# Principal component analysis

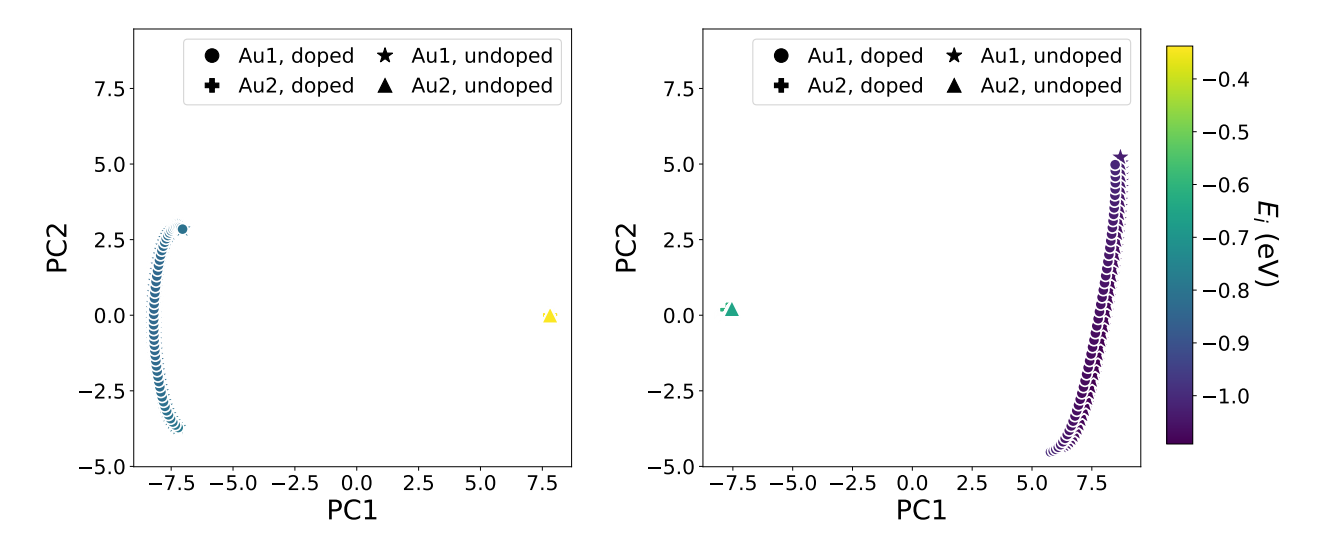


Fig. S2: Coverage of the Au atomic features in latent space. The graph-convoluted Au atomic features extracted from TensorNet (left) and QET (right) for the undoped and Aldoped cases were projected onto the reduced two-dimensional latent space. The directionality reduction is performed using principal component analysis. The heat map indicates the range of the predicted atomic energies  $E_i$ .

## **MatQ Dataset Statistics**

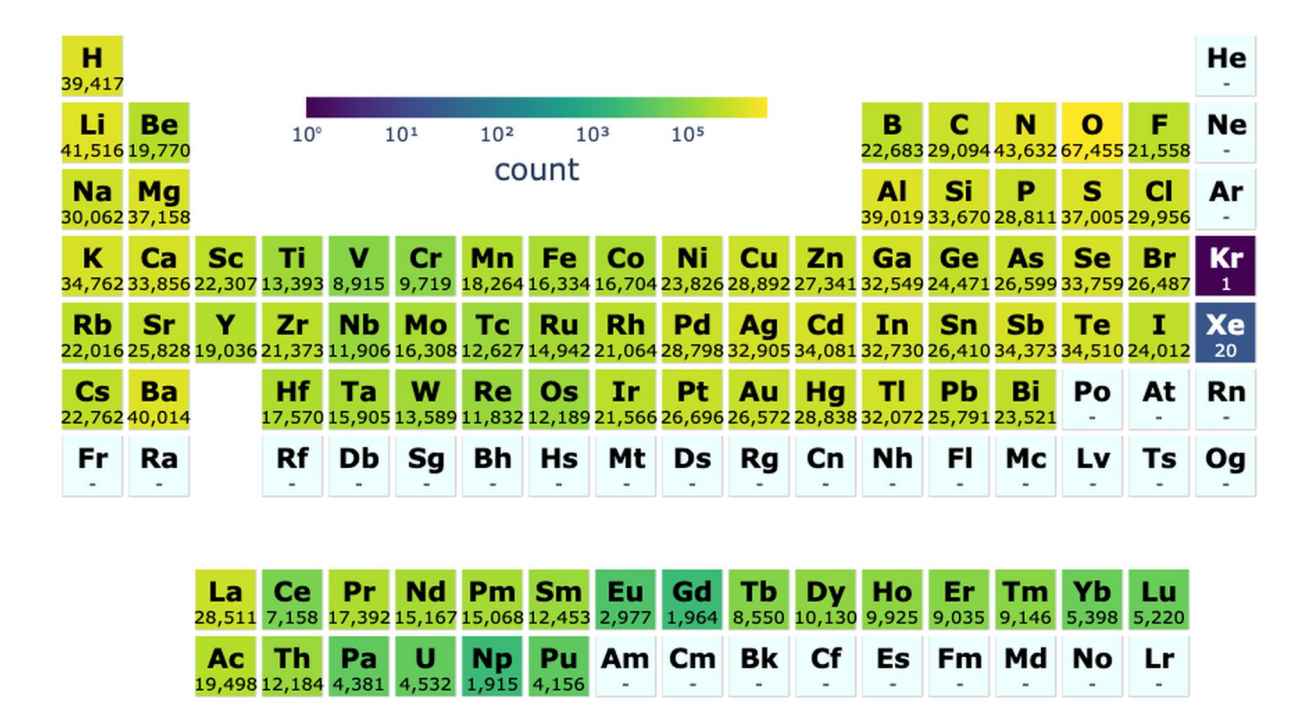


Fig. S3: Elemental coverage of the MatQ dataset. Heatmap of elemental distributions in the dataset. Each cell shows the number of structures containing that element, displayed on a logarithmic scale.

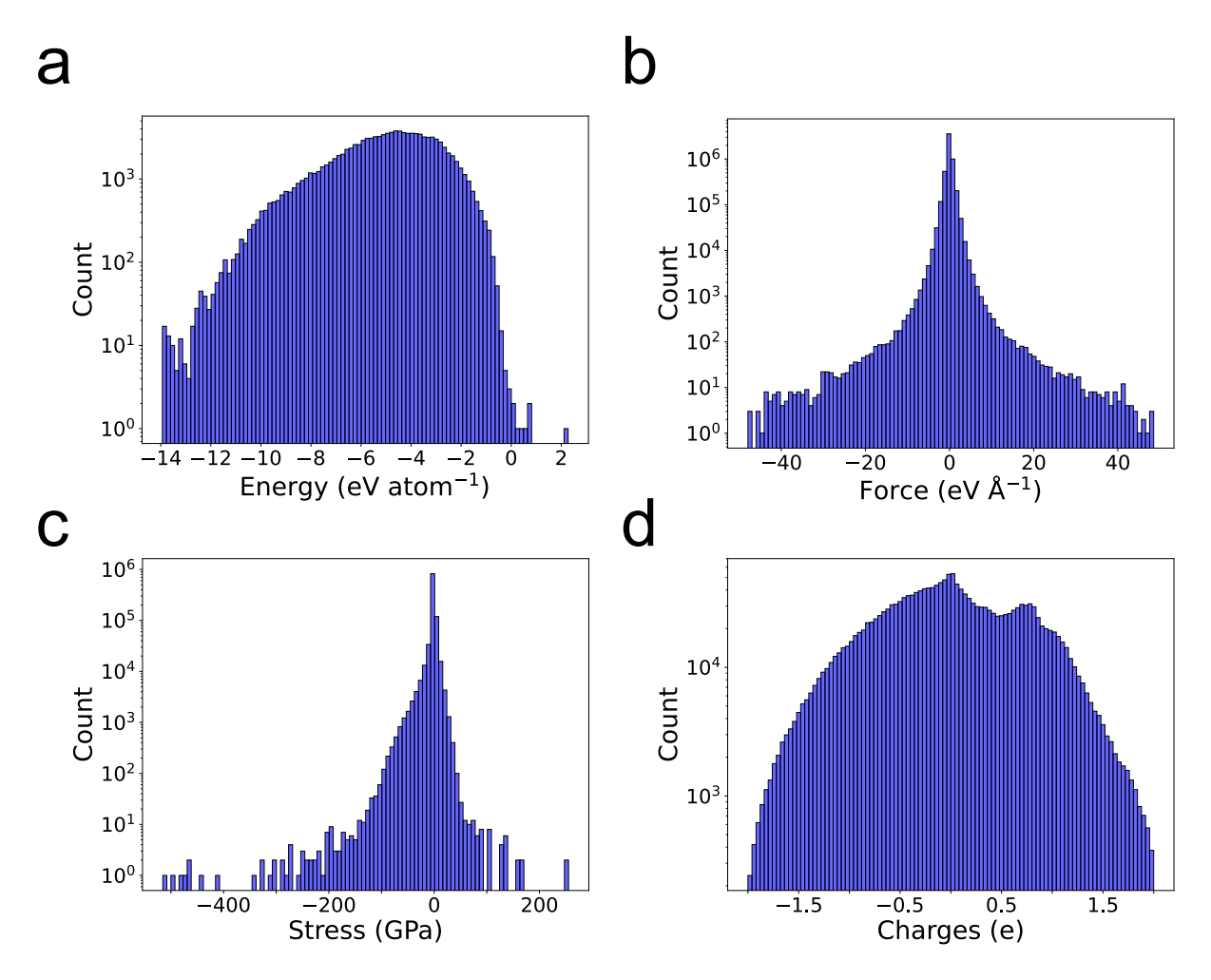


Fig. S4: Distribution of target properties for MatQ dataset. Histograms of the a energies (eV atom<sup>-1</sup>), **b** force components (eV Å<sup>-1</sup>), **c** stress (GPa) and **d** DDEC6 charges (e) for the MatQ dataset.

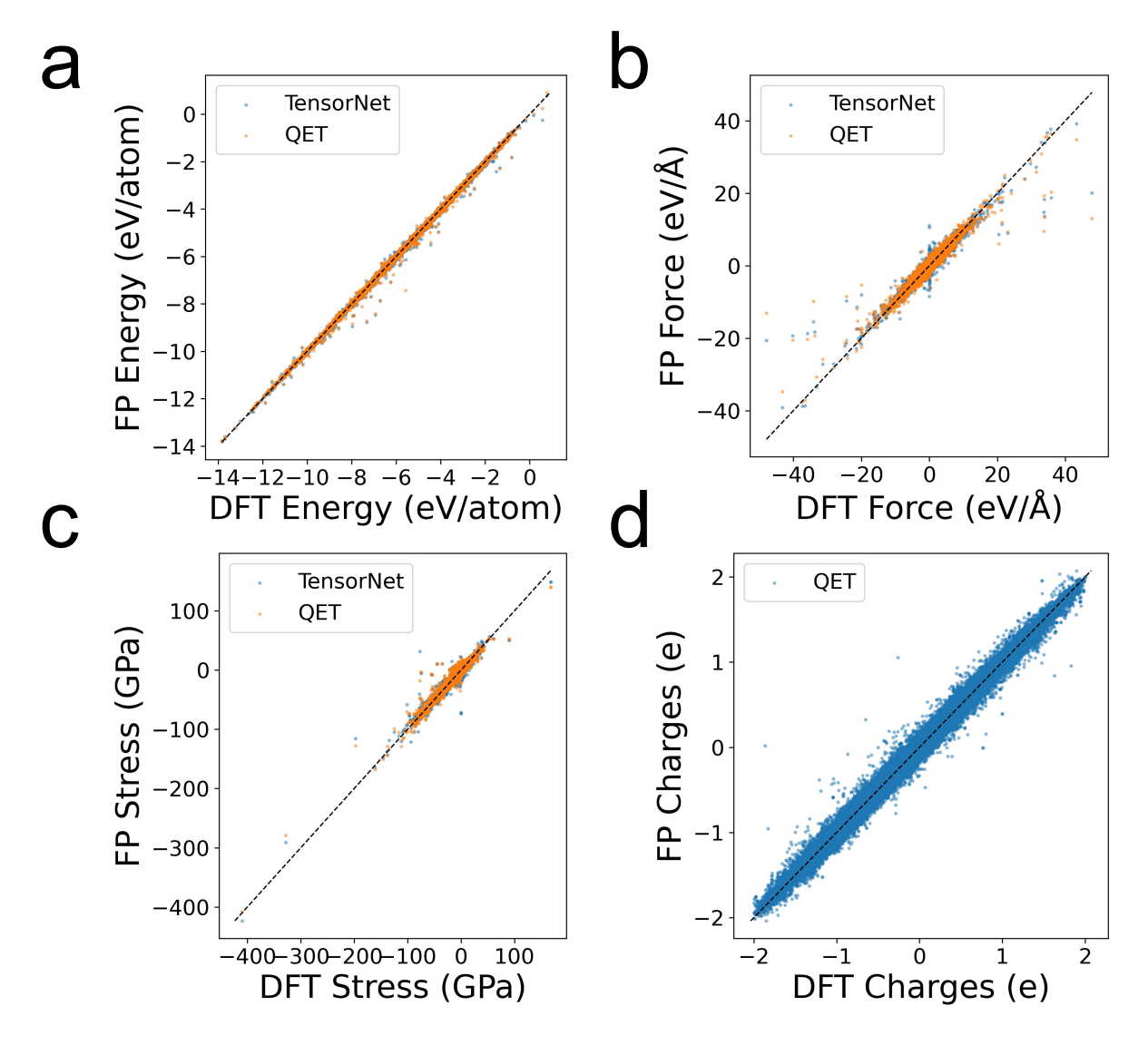


Fig. S5: Performance of foundation potentials trained using Mat-Q dataset. Parity plots for a energies, b forces, c stresses and d charges for the training and validation set.

# Fine-tuning of Li/Li<sub>6</sub>PS<sub>5</sub>Cl

Table S1: Validation errors of fine-tuned foundation potentials on  $\text{Li/Li}_6\text{PS}_5\text{Cl}$  dataset. The root mean square errors (RMSE) of energies (meV atom<sup>-1</sup>), forces (meV Å<sup>-1</sup>), and stresses (GPa) for the validation set were computed using fine-tuned TensorNet and QET MLIPs. The errors calculated with the customized DeepMD are taken from Ref. 1.

RMSE	DeepMD	TensorNet	QET
Energy	5.450	2.816	2.537
Force	93.900	85.549	77.933
Stress	N. A	0.055	0.047

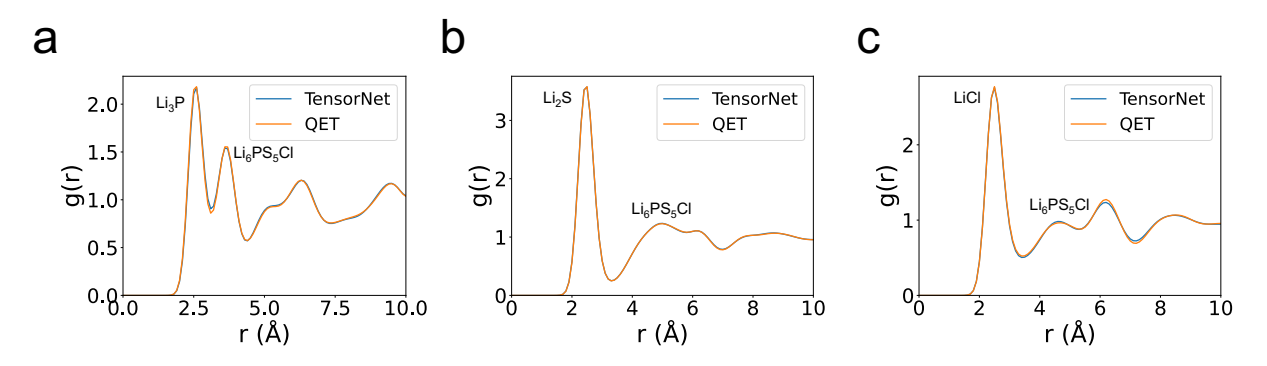


Fig. S6: Local environment of Li atoms in Li/Li<sub>6</sub>PS<sub>5</sub>Cl. Calculated radial distribution functions of a Li-P, b Li-S and c Li-Cl pairs from the last 1 ns of *NVT* MD simulations.

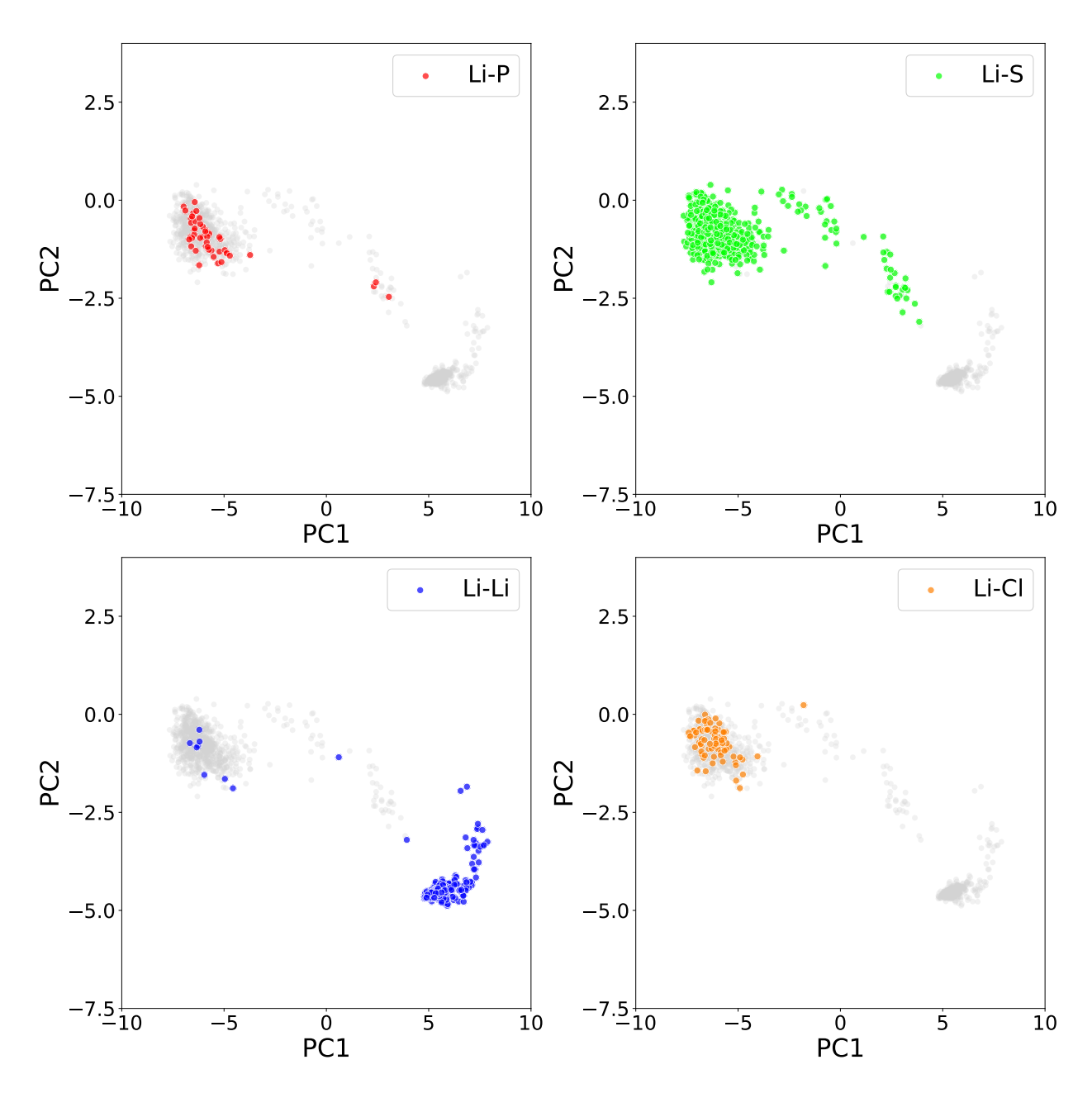


Fig. S7: Correlation between atomic features and local environment of Li atoms in Li/Li<sub>6</sub>PS<sub>5</sub>Cl. The first two principal components extracted from Li atomic features combined with coordination analysis. The dots colored red, green, blue, and orange represent the nearest neighbors of Li atoms, which are P, S, Li, and Cl, respectively.

# References

(1) An, Y.; Hu, T.; Pang, Q.; Xu, S. Observing Li Nucleation at the Li Metal–Solid Electrolyte Interface in All-Solid-State Batteries. *ACS nano* **2025**, *19*, 14262–14271.